Available online at www.sciencedirect.com
ScienceDirect
Trans. Nonferrous Met. Soc. China 30(2020) 191−199
Transactions of Nonferrous Metals Society of China
www.tnmsc.cn

Structural, optical properties and optical modelling of hydrothermal chemical growth derived ZnO nanowires

Hin On CHU[1], Quan WANG[2], Yong-jing SHI[3], Shi-geng SONG[1], Wei-guo LIU[2], Shun ZHOU[2], Des GIBSON[1], Yahya ALAJLANI[4], Cheng LI[5]

1. Institute of Thin Films, Sensors and Imaging, University of the West of Scotland, Paisley, PA1 2BE, United Kingdom;
2. Institute of Optoelectronic Engineering, Xi'an Technological University, Xi'an 710021, China;
3. School of Metallurgy and Material Engineering, Chongqing University of Science and Technology, Chongqing 401331, China;
4. Department of Physics, Faculty of Science, Jazan University, Jazan, Saudi Arabia;
5. School of Energy and Power, Institute of Energy and Power Technology, Changchun Institute of Technology, Changchun 130103, China

Received 14 December 2018; accepted 29 November 2019

Abstract: ZnO nanowire films were produced at 90 °C using a hydrothermal chemical deposition method, and were characterised with scanning electron microscopy, optical transmission spectrometry and X-ray diffraction. The results showed that the optical band gap is 3.274−3.347 eV. Film porosity and microstructure can be controlled by adjusting the pH of the growth solution. ZnO nanowire films comprise a 2-layer structure as demonstrated by SEM analysis, showing different porosities for each layer. XRD analysis shows preferential growth in the (002) orientation. A comprehensive optical modelling method for nanostructured ZnO thin films was proposed, consisting of Bruggeman effective medium approximations, rough surface light scattering and O'Leary-Johnson-Lim models. Fitted optical transmission of nanostructured ZnO films agreed well with experimental data.
Key words: ZnO; nanowires; hydrothermal synthesis; optical modelling

1 Introduction

Hydrothermal chemical deposition (HCD) is a popular solution processing method for producing complex nanostructured ZnO thin films, owing to its simplicity and wide range of available growth conditions [1−3]. ZnO is a n-type semiconductor, with a direct band-gap energy of 3.2−3.3 eV. Due to its versatility, tunability and wide-range of fabrication options, this material is intensely studied across multiple disciplines. HCD is widely employed in the production of nanostructured ZnO films, with the ability to tune nanostructure, optical and electronic properties by altering chemical growth parameters such as pH, temperature and time. Recent advances in nano-technologies with ZnO involve applications in photovoltaics [4,5], sensors [6−8], medicine [9], piezoelectrics [10] and anode materials for batteries [11−13]. Adjustment to the nanostructure of ZnO via HCD has been studied, and tunability of its physical and optical properties has been reported [3,14−20]. Structure of such ZnO nanowire films can also be controlled by addition of capping agents, such as hexmethyldisilathiane and polyethylene glycol. In this case, surfactants control the metal oxide geometry during nanostructure formation. However, there is limited literature on the optical modelling of complex nanostructured ZnO films.

Corresponding author: Yong-jing SHI; Tel: +86-15902341971; E-mail: yjshi@126.com
DOI: 10.1016/S1003-6326(19)65191-5

Nanostructured films may contain different material regions that develop during film growth, as the area near the film surface is less occupied by ZnO material compared to the film-substrate interface, where an adhesion-promoting layer is used to promote island growth, this may result in relatively high packing density. A novel analytical method for optical modelling of nanostructured thin films was presented, using ZnO nanowire-films as the model system. General modelling approaches are challenged for their accuracy when nanostructured films are concerned because different geometries and porosities affect the optical properties. In this work, optical modelling of such complicated films is achieved using several approximations, including the assumption that the layer of nanostructured ZnO is a mixture of ZnO and air. Nanowire-films tend to produce a composite type material, as the wires themselves are relatively incoherent and of lower density compared to the regions closer to the substrate. Therefore, careful treatment of optical data with Bruggeman effective medium approximation (EMA) [21] and rough surface scattering modelling [22] is required. These results will enable derivation of constants required for the O'Leary-Johnson-Lim (OJL) model [23], which is then used for the prediction of optical properties, such as transmission and band gaps. Whilst each of these models and approximations have been well-established, there currently have been no reports that combine all three methods for the optical characterisation of ZnO nanowire thin films.

2 Experimental

Zinc nitrate hexahydrate was supplied by Sigma-Aldrich, zinc target (99.9% purity) was from Testbourne Ltd. For these HCD reactions, a simple zinc nitrate solution adjusted with ammonia was used. Zinc nitrate, when heated, naturally decomposes into zinc oxide; adjusting pH with ammonia means that the hydrothermal chemical deposition reaction scheme should be as follows:

$$NH_3+H_2O \rightleftharpoons NH_4^+ + OH^- \quad (1)$$

$$Zn(NO_3)_2+2OH^- \rightarrow Zn(OH)_2+2NO_3^- \quad (2)$$

$$Zn(OH)_2 \xrightarrow[\Delta]{90\ ^\circ C} ZnO+H_2O \quad (3)$$

Alternatively, zinc nitrate is known to thermally decompose into zinc oxide. This process begins from 50 °C; however, a significant thermal decomposition is known to take place at 320 °C [24], which is significantly higher than that used in this study.

2.1 Nanowire preparation

Hydrothermal chemical deposition of ZnO nanowire films was based on the recipe from our previous study [25]. Glass substrates were ultrasonically cleaned (Optimal UCS40) and blown dry with nitrogen. Substrates were then loaded into a magnetron sputtering drum, and the chamber was pumped to a high vacuum. 50 nm thick zinc metal layer was sputtered onto glass using a RF argon plasma (Nordiko 3750 magnetron sputtering system). 20 mmol/L zinc nitrate solution was made up from zinc nitrate hexahydrate and deionised water. Ammonium hydroxide was used to adjust the pH, then substrates with zinc adhesion layers were lowered and sealed in the growth solution. These were then transferred into a preheated water bath, set to 90 °C, for 6 h. After this, samples were rinsed using deionised water and allowed to air dry.

2.2 Characterisation methods

Scanning electron microscopy (SEM) was carried out using a Hitachi S4100 scanning electron microscope, where the cross-sectional images required careful cleaving of the sample with a diamond scribe to produce the necessary cross-sectional surface for inspection. Samples were sputter-coated with a thin layer of Au prior to measurement. X-ray diffraction (XRD) was carried out using a Siemens D5100 diffractometer, in the locked-couple mode, with 2θ measured from 30° to 60°. Optical spectra were acquired using a Perkin Elmer Lambda 40 UV/Vis spectrometer in transmission mode (250−1100 nm).

3 Results and discussion

3.1 Nanowire characterisation

In this study, pH of the growth solution was varied from 8.5 to 10.2 during HCD growth. It was found that within 6 hours HCD growth, no solution below pH 8.5 formed any nanowire structure. When pH value was in excess of 11, the resultant films exhibited poor uniformity, with some etching into the substrate also observed. Figure 1 shows the

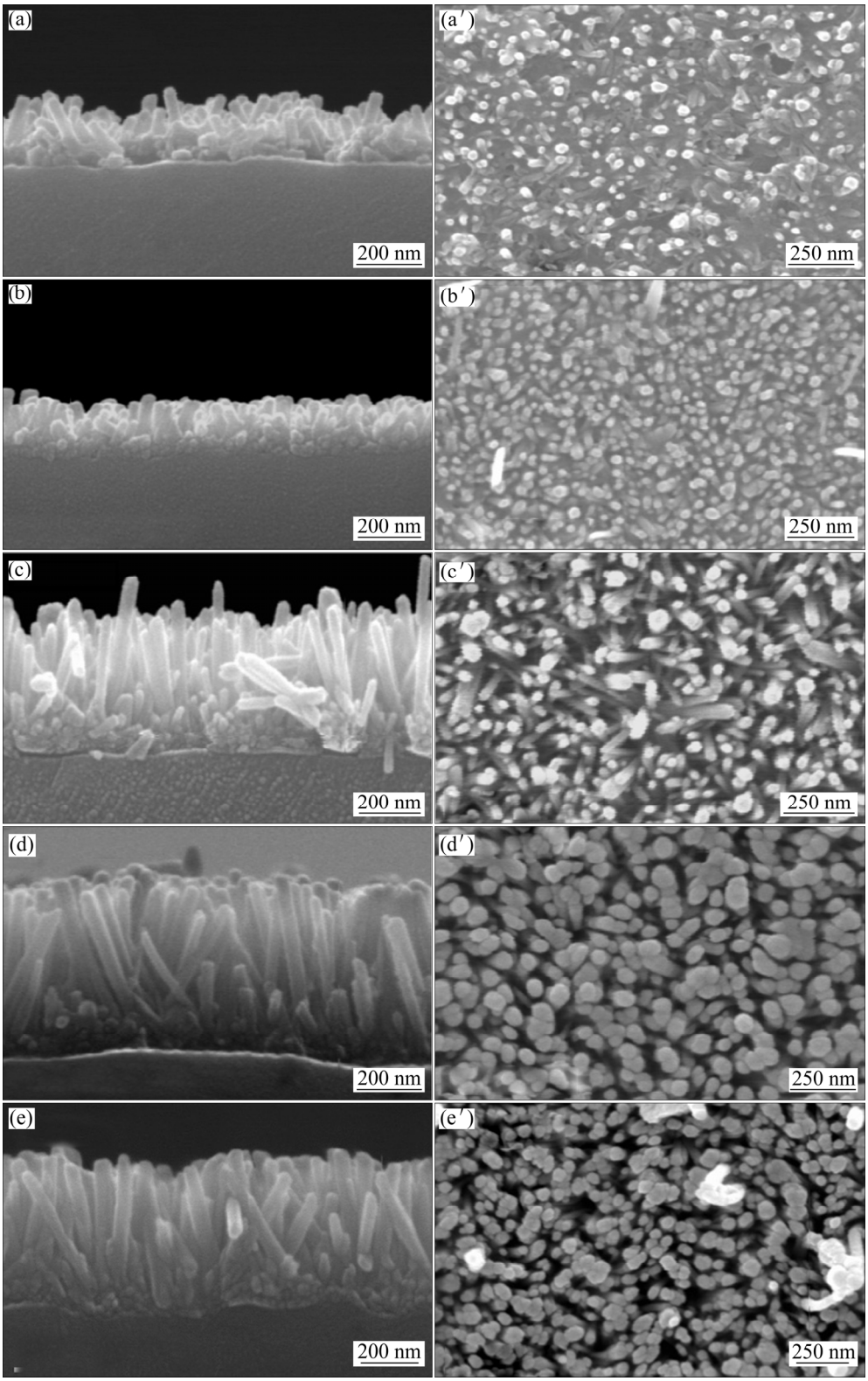

Fig. 1 SEM images of cross-section (a, b, c, d, e) and top-view (a′, b′, c′, d′, e′) of ZnO nanowires grown in solutions of various pH: (a, a′) pH 8.5; (b, b′) pH 9.0; (c, c′) pH 9.5; (d, d′) pH 10.0; (e, e′) pH 10.2

cross-sectional images of the ZnO nanowires grown on the glass substrate. It was noted that increasing pH of the growth solution results in increasing length and thickness of the resultant nanowires. It is speculated that increasing hydroxide concentration promotes displacement of zinc in zinc nitrate, thus speeding up the formation of zinc oxide. Surface morphologies are also seen to alter significantly as

the pH is changed. At pH 8.5, the top-view image shows that loosely packed nanowires have been formed, whereas at higher pH levels, nanorods become longer and more well defined (as seen from the top-view SEM image). It can be seen from the cross-sectional images for all samples, that the region of film nearer to the substrate is more densely packed. This must be taken into consideration during modelling for optical properties, such as film porosity. Porosities were analysed and extracted from the SEM images and expressed as volume fraction. The porosity data are shown in Table 1, and this information is utilised in the EMA.

Table 1 Porosity data derived from SEM image analysis

pH	Layer thickness/nm		Layer volume fraction/%	
	Lower	Upper	Lower	Upper
8.5	35.4	190.8	95.0	58.1
9.0	97.7	72.9	98.0	66.8
9.5	37.6	326.9	96.0	46.4
10.0	166.2	421.7	73.0	39.1
10.2	416.3	159.7	76.8	46.0

To better analyse the porosity of the films, the samples of ZnO nanowire films were approximated to two regions. The region nearer the substrate is defined as the lower layer, and is visibly denser than the upper region which consists of columnar structures; the latter is defined as the upper layer. The latter layer is incoherent whereas the lower layer can be considered to be coherent. Image analysis of the data from SEM provides information regarding the volume fractions, i.e. the ratio of a volume that is occupied with material. This information is required for working with the Bruggeman EMA, which is, in turn, required for theoretical modelling of optical properties of the films. XRD data, as depicted in Fig. 2, show that the ZnO nanowires grown with this method preferentially grow in the (002) orientation. This is consistent with previous reports [25]. The sharp (002) peak indicates that there is high crystallinity in the higher-pH derived samples. It was also observed that increasing pH correlates to an increased (002) peak intensity. Such increase may also be because at higher pH, thicker layers were produced; thus there is a greater quantity of material being observed in the XRD. These trends in crystallinity and film structure may lead to observable changes in optical properties.

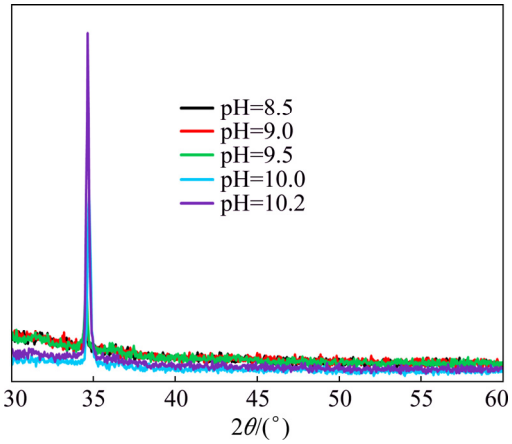

Fig. 2 XRD patterns of ZnO nanowires grown on glass substrate, measured with locked-couple mode in HCD growth solutions with different pH

From the diffraction data, it is possible to obtain the crystal grain size trend with the Scherrer equation (1). So long as the domains do not exceed 100 nm, at such scales the equation is not valid.

$$\tau = \frac{\chi\lambda}{\beta\cos\theta} \tag{4}$$

where τ is the crystal grain size, χ is a shape factor, (set to be 0.89 in this case), λ is the wavelength of incident radiation, β is the full width at half maximum (FWHM) of a known peak in radians and θ is the Bragg angle for the peak FWHM used. From this, Table 2 is obtained and the trend of increasing crystal grain size with increasing pH can be easily observed.

Table 2 Crystal grain size obtained using Scherrer equation for ZnO nanowires

pH	Peak position/(°)	FWHM/(°)	Crystal grain size/nm
8.5	34.51	0.27	60.99
9.0	34.51	0.25	66.40
9.5	34.73	0.23	71.63
10.0	34.54	0.21	76.95
10.2	34.66	0.20	80.75

3.2 Proposed theoretical optical model

Nanowire ZnO film has a complex structure and, so, to analyse optical measurements, a suitable

optical model needs to be established. The model includes two layers to address the mixture of different porosities in the film (as seen in Fig. 1, lower layer is the denser layer and upper layer is the porous nanorods), light scattering from rough surfaces, and to account for semiconductor optical absorption. Then, the OJL model is used to find the band gap energies in semiconductors, as non-perfect crystal materials introduce tail-states that affect the band gap.

3.2.1 Bruggeman effective medium approximation

Bruggeman effective medium approximation is used to model the effect of having multiple components in the optical thin film. This is a popular approach for dielectric constant averaging, which uses volume fraction weighted average. SEM results showed the thickness of each component, assigning the nanowire layer as the mix top layer. The denser, lower ZnO film layer should be treated differently from the nanowire part of the film, which is visibly more porous. From the SEM image analysis, the area data for volume fraction and film thickness are derived. These allow the volume fractions (f_i) to be calculated and from this, the dielectric constants (ε) can be derived using the EMA (Eq. (5)).

$$\sum_i f_i \frac{\varepsilon_i - \varepsilon}{\varepsilon_i - 2\varepsilon} = 0 \tag{5}$$

For these films, i=2 and f_2=1−f_1, then the polynomial in Eq. (5) becomes Eq. (6):

$$-2\varepsilon^2+[3f_1(\varepsilon_1-\varepsilon_2)+2\varepsilon_2-\varepsilon_1]\varepsilon+\varepsilon_1\varepsilon_2=0 \tag{6}$$

Equation (6) is now appropriate for composite materials, such as ZnO nanowire films.

3.2.2 Rough surface light scattering

In order to derive surface roughness parameters required for fitting the band-gap data, the model used is adapted from studies by BENNETT and PORTEUS [26] and DAVIES [27].

Firstly, total integrated scattered light (S_{TIS}) is defined by

$$S_{TIS} = 1 + \frac{R_s}{R_t} \tag{7}$$

where R_s and R_t are the specular and total reflectances, respectively. S_{TIS} can also be defined as the ratio of the diffuse reflectance (R_d) to the total reflectance.

Equation (8) gives the fraction of total reflected radiant power of a specular beam off a rough surface [26,27].

$$\frac{R_s}{R_t} = \exp\left[-\left(\frac{4\pi\cos\theta_i\sigma}{\lambda}\right)^2\right] \tag{8}$$

where θ_i is the incident angle, σ is the root-mean-square surface roughness and λ is the wavelength of the incident light.

Combining Eqs. (7) and (8), S_{TIS} can be expressed as

$$S_{TIS} = 1 - \exp\left[-\left(\frac{4\pi\cos\theta_i\sigma}{\lambda}\right)^2\right] \tag{9}$$

Therefore, for normal incidence (θ_i is 0° and $\cos\theta_i$=1) and very small σ, the following approximation can be obtained using the Taylor expansion:

$$\frac{R_s}{R_t} = 1 - S_{TIS} \approx 1 - \left(\frac{4\pi\sigma}{\lambda}\right)^2 \tag{10}$$

where R_t is the total reflection from a surface, it is also the reflectance from a smooth surface. In this study, transmission results were measured, thus it is necessary to change the equations from reflectance to transmittance. It is possible to infer the transmittance equation from Eq. (10):

$$\frac{T_s}{T_t} \approx C_2 - \left(\frac{4\pi C_1}{\lambda}\right)^2 \tag{11}$$

where T_s and T_t are specular transmittance and total transmittance, respectively; C_2 is an offset constant; C_1 is a roughness parameter which reflects extent of light scattering. The constants can be obtained by fitting the experimental optical transmission data.

3.2.3 O'Leary-Johnson-Lim (OJL) model

In a perfect crystal system, the electronic band gap can be expressed as E_g=V_c–V_v, where V_v and V_c are ground state energies for the valence and conduction bands, respectively. However, in amorphous semiconductors and defected crystal systems, lack of long-range order will affect the band gap properties. The OJL model takes into account the tail-states that arise from these amorphous phases. It is assumed that in a perfect crystal, density of states follows a parabolic nature [23]. This leads to the assumption for conduction-band DOS function (Eq. (12)), and valence-band DOS function (Eq. (13)). Such that in a perfect crystal, the disorderliness constant $\gamma_c \to 0$ results in Eq. (14).

$$N_cE=\frac{\sqrt{2}m^{3/2}}{\pi^2\hbar^3}\begin{cases}\sqrt{E-V_{c'}}, E\geq V_c+\gamma_c/2\\ \sqrt{\gamma_c/2}\exp(-\frac{1}{2})\exp\left(\frac{E-V_c}{\gamma_c}\right), \\ \quad E<V_c+\gamma_c/2\end{cases} \tag{12}$$

$$N_vE=\frac{\sqrt{2}m^{3/2}}{\pi^2\hbar^3}\begin{cases}\sqrt{\gamma_v/2}\exp(-\frac{1}{2})\exp\left(\frac{V_v-E}{\gamma_v}\right), \\ \quad E\geq V_v+\gamma_v/2\\ \sqrt{V_v-E},\ E<V_v+\gamma_v/2\end{cases} \tag{13}$$

$$N_cE\rightarrow\frac{\sqrt{2}m_c^{*3/2}}{\pi^2\hbar^3}\begin{cases}\sqrt{E-V_{c'}}, E\geq V_c\\ 0,\ E<V_c\end{cases} \tag{14}$$

where N_cE and N_vE are the density of states functions; m_c and m_v are the density of states effective masses for their respective bands; V_c and V_v are the disorderliness band edges; γ_c and γ_v represent the breadth of the band tails; $V_c+\gamma_c/2$ and $V_v-\gamma_v/2$ correspond with the transition point between the square root and linear-exponential distribution of states. Using the joint-density of states (JDOS, $\Im(\hbar\omega)$), this is integrated for all energies and energetic transitions (Eq. (11). Using optical transition matrix, the absorption coefficient (α) can be obtained and therefore the extinction coefficient (k) can be calculated. Furthermore, applying the Kramers−Kronig relations for dielectric functions, the refractive index (n) can then be derived:

$$\Im(\hbar\omega)=\int_{-\infty}^{\infty}N_cEN_v(E-\hbar\omega)\mathrm{d}E \tag{15}$$

Thus, the necessary optical property parameters are derived and may be compared to measure optical transmittance data. The model and analysis presented here may provide better analysis of ZnO films for future applications, such as for ZnO gas sensors [28].

3.3 Optical data fitting

Transmittance data from the optical measurements were compared with simulated data. Figure 3 shows that theoretically derived optical transmission data are in good agreement with those which were measured. Different pH values of the solutions used during film growth affect the wavelength at which the transmittance sharply drops. Overall transmittance is lower for nanowires grown at higher pH; this is likely due to the increased growth rate with increased pH, as opposed to varying optical band gaps affecting transmittance. The simulations showed that for differing pH conditions, the samples showed only small changes in their band gap energies. This is not to say that pH changes do not affect the fitted band gap energies; however, the observed changes in band gap energies are small and may be due to reasons other than changes in pH alone.

The band gap energies obtained via data fittings are shown in Table 3.

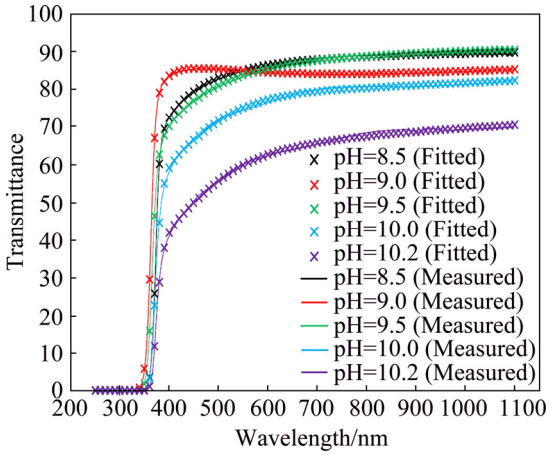

Fig. 3 Transmittance data for ZnO nanowires grown at various pH and corresponding fitted transmittance data, ranging from 250 to 1100 nm

Table 3 Band gap energies of ZnO films grown at various pH

pH	E_g/eV	Crystal grain size/nm	Radius/nm	C_1/nm
8.5	3.274	60.99	30.50	1.012
9.0	3.347	66.40	33.20	3.352
9.5	3.343	71.63	35.82	3.176
10.0	3.335	76.95	38.48	12.009
10.2	3.318	80.75	40.38	14.440

XRD results indicate a clear relationship between pH and the crystal grain size. Similarly, there is a general trend between crystal grain size and band gap energies with barring one result (pH=8.5), as shown in Fig. 4. It was also observed, that as the pH increased, so did the roughness which was indicated by the increasing C_1.

Band gap energy shifts with decreasing crystallite size may seem familiar to what is observed with quantum confinement effects [29]. However, our crystal grain sizes are too large to be thus explained. Quantum confinement effects are not the only explanation for changes to band gap

energies, as crystal grain size dependence on the band gap has been previously reported by BENRAMARCHE et al [30], where the crystal grain size is significantly larger than the ZnO Bohr radius, but changes in band gap energies were observed. For example, while strain on ZnO has been known to alter the band gap energy, simulations conclude that these effects diminish once particle size is 2.4 nm or greater [31]. Other literatures [32−34] also reported nanorods with changed optical band gaps that were not exclusively due to quantum confinement effects. Such as a report that found mechanically bent ZnO nanorods exhibited changes in stress that led to observable change in optical band gap energies. Although it is difficult to conclude the reason for the trend between crystal grain size and band gap energies, it is confirmed that crystal grain size does indeed affect the band gap energies even at large dimensions.

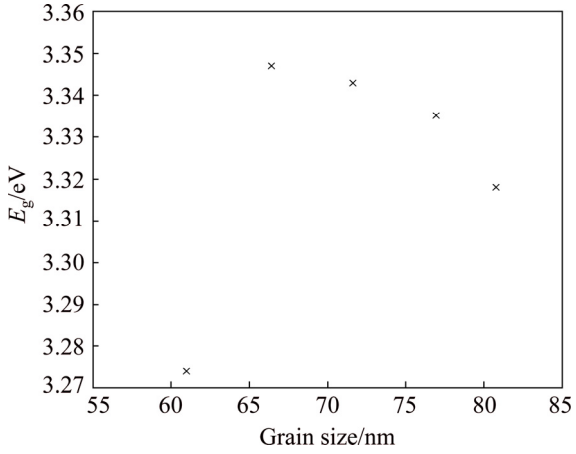

Fig. 4 Relationship between estimated crystallite size and derived band gap energy

4 Conclusions

(1) Varying the pH of the solution used in the deposition of ZnO films significantly altered their optical properties. The theoretical model proposed agrees well with the experimental data. The ability to tune film structure and surface roughness via variation of pH is also demonstrated.

(2) ZnO nanowire films consist of two main layers: one upper porous nanowire layer and one visibly denser film layer nearer to the substrate. Higher pH conditions result in faster hydrothermal chemical deposition; however, a non-linear relationship with the estimated volume fractions was observed.

(3) Fitted dielectric constants show good agreement with experimental measurements; the model and analysis presented here may therefore provide better analysis of ZnO films for future applications, such as ZnO gas sensors.

(4) XRD analysis suggests a clear relationship between crystal grain size and band gap energy.

(5) Optical characterisation of nanostructured ZnO nanowire films using a combination of Bruggeman effective medium approximation, rough surface light scattering and O'Leary-Johnson-Lim modelling was achieved.

Acknowledgements

Authors would like to acknowledge Dr. Liz Porteous for her help with SEM imaging, Dr. Ross Birney with discussion and proofing and Mr. Charles McGinness for his help with providing chemicals.

References

[1] BARUAH S, DUTTA J. Hydrothermal growth of ZnO nanostructures [J]. Science and Technology of Advanced Materials, 2009, 10: 013001.

[2] WANG J, CHEN R, XIANG L, KOMARNENI S. Synthesis, properties and applications of ZnO nanomaterials with oxygen vacancies: A review [J]. Ceramics International, 2018, 44: 7357−7377.

[3] XU S, CHENG C, GUO W, HE Y, HUANG R, DU S, WANG N. Tuning the optical and electrical properties of hydrothermally grown ZnO nanowires by sealed post annealing treatment [J]. Solid State Communications, 2013, 160: 41−46.

[4] DEARDEN C A, WALKER M, BEAUMONT N, HANCOX I, UNSWORTH N K, SULLIVAN P, MCCONVILLE C F, JONES T S. High voltage hybrid organic photovoltaics using a zinc oxide acceptor and a subphthalocyanine donor [J]. Physical Chemistry Chemical Physics: PCCP, 2014, 16: 18926−18932.

[5] DJURISIC A B, LIU X, LEUNG Y H. Zinc oxide films and nanomaterials for photovoltaic applications [J]. Physica Status Solidi (RRL)−Rapid Research Letters, 2014, 8: 123−132.

[6] BIASOTTO G, RANIERI M, FOSCHINI C, SIMÕES A, LONGO E, ZAGHETE M. Gas sensor applications of zinc oxide thin film grown by the polymeric precursor method [J]. Ceramics International, 2014, 40: 14991−14996.

[7] KUMAR R, AL-DOSSARY O, KUMAR G, UMAR A. Zinc oxide nanostructures for NO_2 gas-sensor applications: A review [J]. Nano-Micro Letters, 2015, 7: 97−120.

[8] MOHD FUDZI L, ZAINAL Z, LIM H N, CHANG S K, HOLI A M, SARIF MOHD ALI M. Effect of temperature and growth time on vertically aligned ZnO nanorods by

simplified hydrothermal technique for photoelectrochemical cells [J]. Materials, 2018, 11: 1−13.

[9] ZHANG Y, NAYAK T R, HONG H, CAI W. Biomedical applications of zinc oxide nanomaterials. [J]. Current Molecular Medicine, 2013, 13: 1633−45.

[10] NOUR E S, NUR O, WILLANDER M. Zinc oxide piezoelectric nano-generators for low frequency applications [J]. Semiconductor Science and Technology, 2017, 32: 064005.

[11] LI J, ZHAO T, SHANGGUAN E, LI Y, LI L, WANG D, WANG M, CHANG Z, LI Q. Enhancing the rate and cycling performance of spherical ZnO anode material for advanced zinc-nickel secondary batteries by combined in-situ doping and coating with carbon [J]. Electrochimica Acta, 2017, 236: 180−189.

[12] ZHANG J, GU P, XU J, XUE H, PANG H. High performance of electrochemical lithium storage batteries: ZnO-based nanomaterials for lithium-ion and lithium−sulfur batteries [J]. Nanoscale, 2016, 8: 18578−18595.

[13] SHEN X, MU D, CHEN S, WU B, WU F. Enhanced electro-chemical performance of ZnO-loaded/porous carbon composite as anode materials for lithium ion batteries [J]. ACS Applied Materials & Interfaces, 2013, 5: 3118−3125.

[14] PETROVIĆ Ž, RISTIĆ M, MARCIUŠ M, IVANDA M, DURINA V, MUSIĆ S. Hydrothermal processing of electrospun fibers in the synthesis of 1D ZnO nanoparticles [J]. Materials Letters, 2016, 176: 278−281.

[15] PARK J S, MAHMUD I, SHIN Y C, CHOI J C, KIM B, SHIN H J, CHOI Y S, KIM H R. Influence of substrate surface energy and surfactant on crystalline morphology and surface defect density in hydrothermally-grown ZnO nanowires [J]. Materials Science in Semiconductor Processing, 2018, 77: 64−73.

[16] ALZOUBI T, QUTAISH H, AL-SHAWWA E, HAMZAWY S. Enhanced UV-light detection based on ZnO nanowires/ graphene oxide hybrid using cost-effective low temperature hydrothermal process [J]. Optical Materials, 2018, 77: 226−232.

[17] MUCHUWENI E, SATHIARAJ T, NYAKOTYO H. Hydrothermal synthesis of ZnO nanowires on rf sputtered Ga and Al co-doped ZnO thin films for solar cell application [J]. Journal of Alloys and Compounds, 2017, 721: 45−54.

[18] MUCHUWENI E, SATHIARAJ T, NYAKOTYO H. Effect of annealing on the microstructural, optical and electrical properties of ZnO nanowires by hydrothermal synthesis for transparent electrode fabrication [J]. Materials Science and Engineering B, 2018, 227: 68−73.

[19] XIE F, HU W, NING D, ZHUO L, DENG J, LU Z. ZnO nanowires decoration on carbon fiber via hydrothermal synthesis for paper-based friction materials with improved friction and wear properties [J]. Ceramics International, 2018, 44: 4204−4210.

[20] IBUPOTO Z, KHUN K, ERIKSSON M, ALSALHI M, ATIF M, ANSARI A, WILLANDER M. Hydrothermal growth of vertically aligned ZnO nanorods using a biocomposite seed layer of ZnO nanoparticles [J]. Materials, 2013, 6: 3584−3597.

[21] STROUD, D. The effective medium approximations: Some recent developments [J]. Superlattices and Microstructures, 1998, 23: 567−573.

[22] HARVEY J E, CHOI N, SCHROEDER S, DUPARRE A. Total integrated scatter from surfaces with arbitrary roughness, correlation widths, and incident angles [J]. Optical Engineering, 2012, 51: 013402.

[23] O'LEARY S K, JOHNSON S R, LIM P K. The relationship between the distribution of electronic states and the optical absorption spectrum of an amorphous semiconductor: An empirical analysis [J]. Journal of Applied Physics, 1997, 82: 3334−3340.

[24] CSERI T, BEKASSY S, KENESSEY G, LIPTA G, FIGUERAS F. Characterization of metal nitrates and clay supported metal nitrates by thermal analysis [J]. Thermochimica Acta, 1996, 288: 137−154.

[25] ALAJLANI Y, PLACIDO F, GIBSON D, CHU H O, SONG S, PORTEOUS L, MOH S. Nanostructured ZnO films prepared by hydrothermal chemical deposition and microwave-activated reactive sputtering [J]. Surface and Coatings Technology, 2015, 290: 16−20.

[26] BENNETT H E, PORTEUS J O. Relation between surface roughness and specular reflectance at normal incidence [J]. Journal of the Optical Society of America, 1961, 51: 123−129.

[27] DAVIES H. The reflection of electromagnetic waves from a rough surface [J]. Proceedings of the IEE, Part IV: Institution Monographs, 1964, 101: 209−214.

[28] ZUBAIR N, AKHTAR K. High performance room temperature gas sensor based on novel morphology of zinc oxide nanostructures [J]. Transactions of Nonferrous Metals Society of China, 2019, 29: 143−156.

[29] MAROTTI R, GIORGI P, MACHADO G, DALCHIELE E. Crystallite size dependence of band gap energy for electrodeposited ZnO grown at different temperatures [J]. Solar Energy Materials and Solar Cells, 2006, 90: 2356−2361.

[30] BENRAMACHE S, BELAHSSEN O, ARIF A, GUETTAF A. A correlation for crystallite size of undoped ZnO thin film with the band gap energy-precursor molarity-substrate temperature [J]. Optik, 2014, 125: 1303−1306.

[31] YANG Y, YAN X H, XIAO Y, LU D. Size-dependent strain effects on electronic and optical properties of ZnO nanowires [J]. Applied Physics Letters, 2010, 97: 033106.

[32] WEI B, ZHENG K, JI Y, ZHANG Y, ZHANG Z, HAN X. Size-dependent bandgap modulation of ZnO nanowires by tensile strain [J]. Nano Letters, 2012, 12: 4595−4599.

[33] SHAO R W, ZHENG K, WEI B, ZHANG Y F, LI Y J, HAN X D, ZHANG Z, ZOU J. Bandgap engineering and manipulating electronic and optical properties of ZnO nanowires by uniaxial strain [J]. Nanoscale, 2014, 6: 4936−4941.

[34] VAZINISHAYAN A, LAMBADA D R, YANG S, ZHANG G, CHENG B, WOLDU Y T, SHAFIQUE S, WANG Y, ANASTASE N. Effects of mechanical strain on optical properties of ZnO nanowire [J]. AIP Advances, 2018, 8: 025306.

水热法制备的 ZnO 纳米线的微结构、光学性质以及光学模型

朱宪安[1]，王 泉[2]，石永敬[3]，宋世庚[1]，刘卫国[2]，
周 顺[2]，Des GIBSON[1]，Yahya ALAJLANI[4]，李 成[5]

1. Institute of Thin Films, Sensors and Imaging, University of the West of Scotland, Paisley, PA1 2BE, United Kingdom;
2. 西安工业大学 光电工程学院，西安 710021；
3. 重庆科技学院 冶金与材料工程学院，重庆 401331；
4. Department of Physics, Faculty of Science, Jazan University, Jazan, Saudi Arabia；
5. 长春工程学院 能源动力工程学院，长春 130103

摘 要：在 90 °C 的温度环境下，采用水热化学沉积法制备 ZnO 纳米线薄膜，然后用扫描电子显微镜、透射光谱和 X 射线衍射等技术对所制备的纳米薄膜进行表征。结果表明，制备的纳米 ZnO 薄膜的光学带隙在 3.274 到 3.347 eV 之间。调节 pH 值可以控制膜的孔隙率和显微结构。SEM 照片清楚地显示两层结构，且这两层的空隙率不同。XRD 结果显示(002)取向的优先生长。针对纳米结构的 ZnO 薄膜建立一个完整的光学模型，包括 Bruggeman 有效介质近似、粗糙表面的光散射和 O'Leary-Johnson-Lim 带间吸收模型。利用此光学模型，拟合实验测量的纳米结构 ZnO 薄膜的透射光谱，拟合结果同实验结果具有很高的一致性。

关键词：ZnO；纳米线；水热制备；光学模型

(Edited by Xiang-qun LI)